The role of the Indian Ocean sector for prediction of the coupled Indo-Pacific system: Impact of atmospheric coupling

E.C. Hackert[1], A.J. Busalacchi[2,3], J. Carton[3], R. Murtugudde[1,3], P. Arkin[1], and M. N. Evans[1,4]

[1]Earth System Science Interdisciplinary Center, University of Maryland, College Park, Maryland, USA.

[2]University Corporation for Atmospheric Research, Boulder, Colorado, USA.

[3]Department of Atmospheric and Oceanic Sciences, University of Maryland, College Park, Maryland, USA.

[4]Department of Geology, University of Maryland, College Park, Maryland, USA.

Corresponding author: Eric Hackert (ehackert@essic.umd.edu)

Key Points:

- Indian Ocean teleconnections generate off-equatorial easterly winds and curl that act to amplify the oceanic Rossby waves in the Pacific
- These Rossby waves eventually positively impact the eastern Pacific via reflected western boundary then equatorial Kelvin waves
- Coupled hindcasts that include interannual forcing in the Indian Ocean significantly improve ENSO prediction skill from 3-9 months

12/13/2016

Abstract

Indian Ocean (IO) dynamics impact ENSO predictability by influencing wind and precipitation anomalies in the Pacific. To test if the upstream influence of the IO improves ENSO validation statistics, a combination of forced ocean, atmosphere, and coupled models are utilized. In one experiment, the full tropical Indo-Pacific region atmosphere is forced by observed interannual SST anomalies. In the other, the IO is forced by climatological SST. Differences between these two forced atmospheric model experiments spotlight a much richer wind response pattern in the Pacific than previous studies that used idealized forcing and simple linear atmospheric models. Weak westerlies are found near the equator similar to earlier literature. However, at initialization strong easterlies between 30^{o}S to 10^{o}S and 0^{o}N to 25^{o}N and equatorial convergence of the meridional winds across the entire Pacific are unique findings from this paper. The large-scale equatorial divergence west of the dateline and northeasterly-to-northwesterly cross-equatorial flow converging on the equator east of the dateline in the Pacific are generated from interannual IO SST coupling. In addition, off-equatorial downwelling curl impacts large-scale oceanic waves (i.e. Rossby waves reflect as western boundary Kelvin waves). After 3 months, these downwelling equatorial Kelvin waves propagate across the Pacific and strengthen the NINO3 SST. Eventually Bjerknes feedbacks take hold in the eastern Pacific which allows this warm anomaly to grow. Coupled forecasts for NINO3 SST anomalies for 1993-2014 demonstrate that including interannual IO forcing significantly improves predictions for 3-9 month lead times.

1. Introduction

El Niño/Southern Oscillation (ENSO) is the single most important and societally impactful mode of global climate variability on interannual time scales (e.g. [*Lau and Nath*, 2003], [*Glantz*, 2001], [*Horel and Wallace*, 1981]) but its prediction still has much to improve upon (e.g. [*National Academies of Sciences and Medicine*, 2016], [*National Research Council*, 2010]). For example, although six month lead forecasts from June 2014 confidently predicted strong ENSO warm phase conditions based on heat storage anomalies, an event did not develop, with the most likely explanation the failure to predict the absence of coupling between the ocean and the atmosphere [*McPhaden*, 2015].

There are several possibilities for this prediction failure which include 1) initial triggering events (i.e. westerly wind bursts) were out of sync with an amplifying mode and with the typical El Niño development timing (occurring 1 month earlier than for 1997 event) [*Menkes et al.*, 2014], 2) negative feedbacks such as upwelling ocean waves may have damped warm ENSO sea surface temperature anomalies (e.g. as happened for the 2002 event [*Hackert et al.*, 2007]), 3) stronger trade wind easterlies associated with the cool phase of the Pacific Decadal Oscillation (PDO) could have inhibited migration of the precipitation from the warm pool eastward [*Min et al.*, 2015], and 4) Indian Ocean (IO) dynamics may have anchored deep convection over the Indo-Pacific warm pool rather than allowing it to anomalously develop and couple with central/eastern Pacific SST anomalies [*Santoso et al.*, 2012].

Here we focus on the last possibility by isolating the impact of the IO atmosphere on the development of ENSO events. In previous work, [*Wu and Kirtman*, 2004], [*Annamalai et al.*, 2005], and [*Annamalai et al.*, 2010] proposed that cold IO sea surface temperature anomalies (SSTA) could generate an atmospheric Kelvin wave manifesting as equatorial westerly wind anomalies over the western Pacific, deepening the thermocline in the eastern Pacific via large-scale oceanic Kelvin wave processes (e.g. [*Kessler et al.*, 1995]), and enhancing an ongoing El Niño.

[*Wu and Kirtman*, 2004] compared coupled and decoupled general circulation model (CGCM) experiments to test the impact of the IO on ENSO development. They showed that the ENSO variability is reduced by a factor of two when the IO is decoupled (0.56^{o}C to 0.27^{o}C). Composite equatorially averaged SST anomalies over longitude and time for the Pacific show that maximum coupled SST anomalies at 165^{o}W are located 15^{o} east of those observed in the uncoupled experiment (as in [*Yu et al.*, 2002]) and eastern upwelling associated with Kelvin wave arrival is delayed by one month. The dominant period of variability is extended by half a year by decoupling the IO, inconsistent with earlier work of [*Yu et al.*, 2002]. Using a linear atmospheric model and idealized SSTA forcing, [*Wu and Kirtman*, 2004] found that the influence of the IO is via the convective heating and modulation of the Walker circulation. IO SST can induce anomalous Walker circulation over the eastern equatorial IO (EEIO) and western-central Pacific through anomalous heating over the IO. For example, cold IO SST induces development of anomalous westerlies to the east of Indonesia and easterlies to the west, producing the atmospheric Kelvin wave pattern and a weakening of the Walker circulation [*Wu and Kirtman*, 2004]. Therefore, IO SST forcing results indicate a mechanism that can enhance westerlies over the western Pacific resulting in development of stronger El Niño conditions.

Consistent with these results, [*Annamalai et al.*, 2010] find that El Niño is much stronger when occurring with Indian Ocean Dipole Zonal Mode (IODZM) and cold SST over the EIO and in the Indonesian Seas (110^{o}E-140^{o}E, 10^{o}S-0^{o}). Winds are westerly over the Pacific from 130^{o}E east to 120^{o}W and easterly over Indonesia west to the central IO indicating a weaker Walker circulation. The eastern Pacific thermocline deepens and SST warms east of the dateline.

Precipitation is decreased from the central IO to 160^{o}E in the Pacific and increased just east of 160^{o}E and in the western Pacific. Further experiments with the Linear Baroclinic Model (LBM) of [*Watanabe and Jin*, 2003] shows that EIO SST forcing generates an atmospheric Rossby wave signature in the eastern IO but no signal in the Pacific, similar to the idealized forcing of IODZM in [*Annamalai et al.*, 2005]. However the impact of the Indonesian Seas (120^{o}E-160^{o}E, 5^{o}S-5^{o}N) on the atmospheric linear model response is surprisingly strong and far reaching. Cold SST forcing in the Indonesian Seas results in strong negative precipitation anomalies ([*Annamalai et al.*, 2010] Figure 7b) creating an atmospheric Kelvin response that is evident by easterlies over Indonesia and strong westerlies stretching to the east over the western equatorial Pacific.

In summary, the IO can have strong influence for ENSO via atmospheric pathways. Regional coupling of basin-scale IO and Indonesian Seas SSTA force enhanced westerlies over the entire Pacific and increased ENSO forcing. The proposed mechanism is as follows: cold SST over the EIO 1) reduces the normal east/west temperature gradient across the Pacific providing favorable conditions for westerly anomalies to develop, 2) suppresses convection over the Maritime continent and the resulting atmospheric Kelvin wave forces westerlies to the east, 3) leads to convergence of the westerlies that enhance western Pacific precipitation, and 4) results in an increased temperature gradient between Indonesia and the dateline further enhancing westerlies. These westerlies then lead to downwelling oceanic Kelvin waves further enhancing the growth of El Niño. Although [*Annamalai et al.*, 2010] conclude that regional IO SST and heating anomalies are not the primary cause, but rather serve to enhance the development of El Niño, the IO can have strong influences for ENSO via atmospheric teleconnections. Unfortunately, all previous studies (i.e. [*Wu and Kirtman*, 2004], [*Annamalai et al.*, 2005], and

[*Annamalai et al.*, 2010], etc.) used idealized SSTA patterns and simplified linear atmospheric models to show impacts of the IO on the wind field without assessing observed ENSO predictability.

Our approach is to use a combination of ocean-only and coupled models to diagnose the impact of the IO atmospheric teleconnections to ENSO predictability. We will use similar techniques as in previous studies ([*Yu et al.*, 2002], [*Wu and Kirtman*, 2004], [*Annamalai et al.*, 2005], [*Annamalai et al.*, 2010], and [*Santoso et al.*, 2012]) to diagnose the impact of the interannual SSTA forcing in the IO. Namely, we difference results from experiments that fully couple the SSTA throughout the Indo-Pacific region with ones that decouple the IO by forcing with climatological SST in this region. Unlike all previous studies, however, we develop realistic coupled hindcast experiments using realistic interannual anomalies as forcing, and validate the results against observations of forecasted ENSO state. The overriding hypothesis that we wish to test is that the upstream influence of the Indian Ocean improves ENSO predictions through mechanisms associated with the atmospheric bridge as coined by [*Alexander et al.*, 2002]. We will use “atmospheric bridge”, “atmospheric teleconnection” or “atmospheric impact” interchangeably throughout the following text for this impact.

The organization of this paper is as follows. Section 2 covers ocean and coupled models and Section 3 describes the simulations and analysis techniques. Section 4 reports the various model results, Section 5 contains the discussion, and Section 6 summarizes the paper results and provides conclusions.

2. Models

2.1 Ocean Model

The ocean general circulation model (OGCM) that is used in this study is the primitive-equation, sigma-coordinate model with variable depth oceanic mixed layer of *Gent and Cane* [1989]. It is described and validated in a series of simulation studies of circulation in all three tropical ocean basins [*Hackert et al.*, 2001; *Murtugudde and Busalacchi*, 1998; *Murtugudde et al.*, 1996; *Murtugudde et al.*, 1998]. Solar radiation (Earth Radiation Budget Experiment - ERBE) and interannual precipitation from the Global Precipitation Climate Project - GPCP [*Adler et al.*, 2003] are specified externally. Monthly anomalies of the cloud data [NCEP Reanalysis *Kalnay et al.*, 1996] are added to the Interannual Satellite Cloud Climatology Project –ISCCP annual cycle [*Rossow and Schiffer*, 1991] in order to provide a more realistic mean.

Our OGCM uses the hybrid vertical mixing scheme of *Chen et al.* [1994] which combines the advantages of the traditional bulk mixed layer of *Kraus and Turner* [1967] with the dynamic instability model of *Price et al.* [1986]. This allows simulation of all three major processes of oceanic vertical turbulent mixing - atmospheric forcing is related to mixed layer entrainment/detrainment, gradient Richardson number accounts for shear flow, and instantaneous adjustment simulates high frequency convection in the thermocline. The vertical structure consists of a variable depth mixed layer and 19 sigma layers with a deep motionless boundary being specified as $T_{bottom} = 6^{\circ}$C and $S_{bottom} = 35$ PSU.

The ocean model configuration used for all simulations covers the tropical Indo-Pacific basin (34°E -76°W, 30°S-30°N) with a homogeneous 1^{o} longitudinal grid and a variable latitudinal grid (down to 1/3° within 10° of the equator). This resolution is dense enough to allow mesoscale eddies and realistic flow. Surface fluxes are calculated interactively by coupling the OGCM to a thermodynamic atmospheric mixed layer model [*Murtugudde et al.*, 1996] thus allowing feedbacks between SST, SSS, and surface fluxes. The open boundaries are treated as a sponge layer within 10° of the north and south borders smoothly relaxing to World Ocean Atlas 2009 (WOA09 - [*Antonov et al.*, 2010]. Note that this model surface is allowed to vary freely as a natural boundary condition ([*Huang*, 1993]) and only relaxes back to Levitus temperature and salinity ([*Locarnini et al.*, 2010]) within the north and south boundary sponge layers.

The model is spun up from rest using climatological winds with the initial conditions derived from WOA09 data and is allowed to come to equilibrium after 30 years of forcing by the *ECMWF* [1994] analysis climatology. Interannual runs are initialized from this climatological spin-up starting in 1975 and the wind speeds required for sensible and latent heat fluxes are computed from interannual ECMWF 10 m wind converted to stress using the bulk formula (ρ = 1.2 kg/m^3, $C_D = 1.2\text{x}10^3$).

2.2 Atmospheric Model

An intermediate complexity atmospheric general circulation model (AGCM), the International Centre for Theoretical Physics AGCM (nicknamed SPEEDY, for "Simplified Parameterizations, primitivE-Equation DYnamics" - [*Molteni*, 2003]; [*Kucharski et al.*, 2006]) provides an accurate atmospheric model response, yet is highly computationally efficient. We use SPEEDY Version 41, which has global T30 resolution (roughly 3.75°) with 8 standard sigma layers (925 – 30 mb) and surface information. The winds in the tropics have been improved by adding cumulus momentum transport (CMT) to the convective parameterization code using the technique of [*Kim et al.*, 2008]. This technique transports momentum downward within subsidence regions surrounding regions of convection. Adding CMT to the atmospheric model shifts wind and western Pacific precipitation anomalies eastward, which are more in line with observations. In addition, the meridional extent of the wind anomalies is expanded due to the incorporation of the CMT. For example, [*Kim et al.*, 2008] show that 850 mb westerlies during ENSO expand from 15^{o}S-0^{o}N without CMT to 15^{o}S-10^{o}N with CMT. Implementation of CMT has also shown to improve intraseasonal precipitation, SST and winds such as those associated with Madden Julian Oscillations [*Zhou et al.*, 2012]. Hence, effects of the IO on the coupled ENSO system should be distinguishable within SPEEDY simulations via analysis of wind and precipitation anomalies on intraseasonal to interannual timescales.

The winds and precipitation from SPEEDY have similar validation statistics as for other atmospheric models and observations. For example, the mean 925 mb winds of SPEEDY over the tropics closely match the European Centre for Medium-Range Weather Forecasts reanalysis (ERA - [*Gibson et al.*, 1997]). For precipitation, all the major features of the observations (CMAP from [*Xie and Arkin*, 1998]) are reproduced by SPEEDY. However, the SPCZ has less abundant rainfall and relatively more precipitation over the tropical IO [*Molteni*, 2003] and SPEEDY tends to underestimate the zonal wind anomalies associated with ENSO events (see Figure 9 of [*Kroeger and Kucharski*, 2011]). For a full description of latest version of SPEEDY see [*Kucharski et al.*, 2013].

2.3 Coupled Model

Coupling of an intermediate complexity atmospheric model such as SPEEDY is justified since the atmospheric time scale is much shorter than that of the ocean. The SPEEDY AGCM has been successfully coupled with other ocean models for the Pacific (e.g. [*Kucharski et al.*, 2011]), Indian ([*Kucharski et al.*, 2006]), and Indo-Pacific regions ([*Bracco et al.*, 2005]). Similar to the implementation of [*Kroeger and Kucharski*, 2011], we use the technique of anomaly coupling to couple the ocean and atmospheric models. Within the tropical Indo-Pacific region, our ocean model SSTA forces the SPEEDY AGCM. For the rest of the globe, the observed SSTA of HadISST [*Rayner et al.*, 2003] is used and climatological values are used for other atmospheric model boundary conditions such as surface albedo, climatological SST, sea ice, snow depth, vegetation, heat flux parameters, and soil moisture (matching those described in [*Kucharski et al.*, 2013]). The SST anomaly is formulated with respect to the ECMWF/GPCP climate experiment (described in Section 2.1). The atmospheric model is then spun up for 1 month using this SSTA and anomalies of surface zonal and meridional wind stress (τ'_x, τ'_y) and precipitation (*P'*) are formulated with respect to the mean seasonal cycle over 1993-2014 of the similarly forced atmospheric model. These anomalies are subsequently added back to the ECWMF and GPCP climatologies to force the next month of the ocean model simulation. While more efficient than the operational coupled models which use high resolution and more complete atmospheric models, the coupling of SPEEDY nevertheless allows adequate physics to quantify the impact of the atmospheric bridge on ENSO prediction. Using this technique, one year forecasts are completed for each month for 1993-2014.

In order to validate the coupled model, NINO3 SST anomalies are compared against observations. SPEEDY coupled model has significantly better correlation (Figure 1a) and amplitude validation (Figure 1b) than observational persistence after 4 months and 3.5 months, respectively. The correlation of SPEEDY versus observations remains significant at $p<0.05$ (df=35) for 8 month lead times. As a forecast skill comparator, we include the Climate Forecast System Reanalysis Reforecast ([*Saha et al.*, 2014]) as a reference (Figure 1 - black line). These coupled hindcasts are comprised of the atmospheric assimilation/model with resolution ~38 km (detailed in [*Saha et al.*, 2010]) along with the MOM4 ocean model ([*Griffies et al.*, 2004]) with 0.5^o resolution within 30^{o}N-30^{o}S and the Global Ocean Data Assimilation System (GODAS) ocean assimilation ([*Behringer*, 2007]) of all available oceanic in situ data. The CFSRR model was chosen to substantiate our coupled model results since it is a well-known, state of the art, operational coupled model (i.e. the reanalysis, reforecast version of CFSv2). For these long validation runs (i.e. January 1993 to March 2011), correlation between forecasted and observed NINO3 SSTA are equivalent (Figure 1a). For validation by root mean square difference (RMSD), results from our coupled model outperform the CFSRR for all lead times. CFSRR RMSD errors reach 1.4^{o}C at 10 month lead times, whereas SPEEDY coupled model RMSD errors are 1^{o}C for the same lead time. Based on these diagnostics, our coupled model validates at least as well as the NOAA operational model.

3. Simulations and Analysis

3.1 Uncoupled Simulations

SSTA is calculated over 1993-2014 from the ocean model that is forced using all available observed winds, cloudiness, and precipitation (described in Section 2.1). SPEEDY atmosphere-only experiments are then initiated using different ocean model SSTA for the IO basin to isolate the ocean forcing impacts via the atmosphere on the coupled Indo-Pacific system. In this work, the Pacific (abbreviated PAC) is defined as 30^{o}N-30^{o}S, 130^{o}E-70^{o}W and the Indian Ocean (IO) is defined as 30^{o}N-30^{o}S, 30^{o}E-129^{o}E. Outside the tropical Indo-Pacific region, the interannual SSTA from the Hadley Centre (HadISST, [*Rayner et al.*, 2003]) is used to force the global SPEEDY model. Within the Indo-Pacific region, experiments were initiated that are designed to isolate the impact of the IO region surface forcing on the atmosphere.

Table 1 shows the complete set of experiments performed for this study. The experiments either use interannual (i.e. INT) SSTA forcing or climatology seasonal cycle (CLIM) SST separated by basin, PAC and IO. For example, forcing SPEEDY using interannual SSTA for the Pacific and IO is abbreviated as INT_PAC, INT_IO. Following the similar methodology of e.g. [*Wu and Kirtman*, 2004], we subtract the results from these different experiments in order to isolate the impact of the IO sector ocean forcing. Thus, subtracting INT_PAC, CLIM_IO results from INT_PAC, INT_IO will isolate the impact of the IO SSTA via the atmospheric teleconnections to the Pacific.

3.2 Coupled Simulations

A series of coupled experiments designed to isolate the full impact of the interannual IO SSTA forcing is executed. Operationally the same initial conditions are used as for the uncoupled simulations, since the goal is to completely eliminate any potential impacts caused by different initialization. However, within the anomaly coupling procedure we replace the regional SST anomaly with zeros effectively substituting the forecast interannual SST forcing with climatological seasonal cycle values. A series of two 12 month coupled experiments were completed for each month from 1993-2014: for each experiment, a total of 264 12 month runs were completed. The two experiments are 1) INT_PAC, INT_IO (interannual SST anomaly forcing for the Pacific and the IO) and 2) interannual Pacific, climatological IO (INT_PAC, CLIM_IO). As in the uncoupled experiments (section 3.1), the experiments with similar Pacific forcing are compared, e.g. INT_PAC, INT_IO versus INT_PAC, CLIM_IO.

3.3 Analysis Techniques

Unlike all previous similar research, the impact of the IO on ENSO predictability is evaluated using observed quantities. Specifically, the observed NINO3 (5^{o}S-5^{o}N, 90^{o}W-150^{o}W) SSTA from [*Reynolds et al.*, 2002] is used to validate all coupled and forced model results using correlation and RMSD. For correlation, the effective degrees of freedom (df) is calculated using the technique of [*Quenouille*, 1952] (pp. 168-170) with the equation: $df=N/(1.+2.*r_a(1)*r_b(1)+2.*r_a(2)*r_b(2)+2.*r_a(3)*r_b(3))$ where N is original number of observations and r_a and r_b are autocorrelations for time series a and b, respectively for 1, 2, and 3 months lags (indicated by indices). After the effective degrees of freedom are calculated the Students T test is used to establish significance of correlation values. For all statistics, a probability of less than p=0.05 that a correlation is zero will be considered statistically significant and interpretable. In order to test the impact of the IO atmospheric teleconnections to ENSO, forecast lead time correlations will be compared between different coupled model results. Since all experiments are validated against observed SST anomalies, and so share a common variable, these correlations are not independent (known as correlated correlations).

Therefore, the Steiger's Z-test [*Steiger*, 1980] will be utilized to test the significance of the differences between correlations as applied in [*Uehara et al.*, 2014]. The details follow: $Z = \frac{[Z_{aa} - Z_{ba}] * \sqrt{N-3}}{\sqrt{2*[1-r_{aa}]*h}}$ where Z_{ao}, Z_{bo} are Fisher Z transformations of r_{ao} and r_{bo} (the correlation of experiments a and b, respectively versus observations (o), N is the number of observations and r_{ab} is the correlation between the two forecast experiments, a and b, $h = \frac{1-f*rr^2}{1-rr^2}$, $f = \frac{1-r_{aa}}{2*[1-rr^2]}$, and $rr^2 = \frac{r_{aa}+r_{aa}}{2}$. This technique has the benefit of producing a statistic that is normally distributed, so for $|Z| > 1.96$, $p <= 0.05$. In addition, the lead time amplitude of the various forecasts will be validated against observed NINO3 SST anomaly using RMSD. Forecast standard deviation and mean will also be used to compare different forecasts versus observed values. The forecast mean (standard deviation) is simply the mean (standard deviation) across all forecasts, on lead times from 0 to 12 months.

In order to quantify the impact of Kelvin and Rossby wave propagation on El Niño events, sea level anomalies are first converted to geostrophic currents using the methodology of [*Picaut and Tournier*, 1991]. Next, the technique derived by [*Delcroix et al.*, 1994] is used to separate the sea level anomalies geostrophic current data into Kelvin and Rossby components.

4. Results

4.1 Forced Ocean and Atmospheric Model Results

The results of the SPEEDY atmospheric model differences described in Section 3.1 are designed to isolate the impact of the IO and are presented in Figure 2a-f for zonal and meridional wind stresses, precipitation, curl and divergence of the wind stress, respectively. By differencing experiments with full coupling in the IO minus those with decoupled IO, the impact of the variations in the IO summer monsoon is readily apparent for both precipitation and wind stress. For precipitation (Figure 2c), positive anomalies can be seen stretching from the equator to 10^{o}N in the eastern Arabian Sea (AS), at 7^{o}N to 12^{o}N in the Bay of Bengal (BOB), and 10^{o}N to 20^{o}N in the South China Sea (SCS). Abundant rainfall is consistent with convergence of the monsoon flow starting south of the equator as southeasterlies, recurving to southerlies near the equator and decelerating as southwesterlies in the AS, BOB, and SCS (Figure 2d and f). These southwesterlies converge into northeasterlies found north of 10^{o}N in the BOB and SCS. In the Southern Hemisphere, between 10^{o}S and the equator, negative precipitation anomalies are generally found west of 95^{o}E. These precipitation patterns are consistent with the general divergence of the winds in these regions as they feed into the northward monsoon flow. In addition, positive precipitation is found over the southern Indonesian islands between 95^{o}E and 130^{o}E stretching between 12^{o}S to 5^{o}S. This feature is due to the onshore convergence of the westerlies found west of 95^{o}E and is consistent with anomalies that are associated with the transition of the northwest to summer monsoons in boreal spring. In the southwest IO between 25^{o}S-15^{o}S and west of 80^{o}E, a band of positive precipitation is evident just to the east of Madagascar and is the result of southeasterlies to the south converging with northwesterlies to the north (Figure 2f). Warm SST leads to atmospheric advection, enhanced inflow, convergence and abundant atmospheric convection and precipitation. The patterns in the IO are consistent with the anomalies of the monsoon wind and precipitation patterns (those patterns associated with interannual minus climatological seasonal cycle SST forcing in the IO).

In the Pacific, generally positive precipitation anomalies are found off the equator at 5^{o}N, 15^{o}S centered near 160^{o}W (Figure 2c). In addition, positive anomalies are seen in the upwelling region of the eastern equatorial Pacific east of 130^{o}W and in the South Pacific Convergence Zone (SPCZ) at 10^{o}S, 160^{o}E. North of 10^{o}N and south of 20^{o}S, negative precipitation anomalies are simulated. Strong easterly anomalies can be seen between equator and 20^{o}N and south of 15^{o}S across the entire Pacific basin (Figure 2a). North of 20^{o}N, strong westerly anomalies prevail. Between 10^{o}S and the equator, wind differences are generally very weak but westerly. The meridional winds (Figure 2b) converge to roughly 5^{o}S with northerlies to the north and southerlies to south especially east of the dateline. Along 20^{o}N winds are generally divergent for the meridional wind plot.

4.2 Coupled Model Results

The validation of the two coupled simulations versus observed NINO3 SSTA over all 12 month lead times, 1993-2014, is presented in Figure 3a. Both simulations are significantly correlated with observations out to 8 and 5.8 months for INT_PAC, INT_IO and INT_PAC, CLIM_IO, respectively. After 3 month lead times, the correlation of the full coupling begins to outperform the INT_PAC, CLIM_IO coupled simulation. Correlation differences climb to r=0.16 by 7 month lead times. At this time the Steiger Z Test ([*Steiger*, 1980]) shows that the differences are significant (thick dashed line on top x axis in Figure 3a). After that, the differences drop to about r=0.1 out to 10 month lead times when the Figure 3 differences are no longer significant. The important result of this plot is that the interannual forcing of the IO significantly improves coupled forecasts for ENSO. Results for RMSD of simulated versus observed NINO3 SSTA (Figure 3b) are consistent with results for correlation (Figure 3a) and quantify the validation error amplitude.

5. Discussion

Over most of the forecast period and particularly between 3 to 9 month lead times, interannual SST forcing in the IO improves correlation and reduces the RMS differences between observed NINO3 SSTA and those simulated by the fully coupled model. Therefore, these results suggest that including the impacts of the IO atmospheric teleconnection serves to improve the coupled predictability as validated with real observations over 1993 to 2014.

The next step is to examine why the interannual SST forcing of the IO improves the coupled forecasts. Figure 4 shows the mean and standard deviation of the NINO3 SSTA of all the 12 month forecasts from 1993-2014. The mean plot (Figure 4a) shows that the experiment with interannual IO forcing has higher mean values (relative warming signal in the NINO3 region) after 3 months. On the other hand, the INT_PAC, INT_IO and INT_PAC, CLIM_IO standard deviation lines in Figure 4b practically overlay one another. This result is different than that of [*Santoso et al.*, 2012] and [*Wu and Kirtman*, 2004] who found that the IO increased the amplitude of ENSO events. On the contrary, we conclude that the interannual signal in the IO serves to warm the mean state in the eastern Pacific after 3 months rather than impact the variability.

To further diagnose the source of the warming after 3 months, the mean forecast difference, INT_PAC, INT_IO minus INT_PAC, CLIM_IO, is presented for all 12 months of lead times. Equatorial longitude versus time plots track the evolution over the average forecast in Figure 5. Early in the average forecast difference, prior to month 3, easterly winds along the equator between 140^{o}E-160^{o}E and between 180^{o}-140^{o}W (Figure 5c) set off upwelling Kelvin waves (Figure 6a), cooling SSTA (Figure 5a), and inducing westward flow across the entire Pacific (Figure 5d). This is consistent with the general upwelling favorable curl in the initial conditions (Figure 2e) between 15^{o}S-10^{o}N. After this slight upwelling and cooling in the central

Pacific associated with equatorial easterlies, the SST in the NINO3 region begins to warm after 3 month lead times (Figure 5a). In the east, westerlies centered at approximately 130°W generate a downwelling Kelvin wave that arrives at the eastern boundary at month 4 (Figure 6a). At this time the NINO3 region begins to warm (Figure 5a). In the west, westerlies on the equator west of 140°E and near the dateline act in the equatorial Pacific setting off a second downwelling Kelvin wave, which is identified by positive sea level anomaly and eastward flow (Figure 5b, d and Figure 6a) that starts in month 4 and traverses the Pacific and arrives at the eastern boundary by month 6. The cumulative effects of the downwelling Kelvin waves after month 5 are to continue to warm the NINO3 region. For month 6 through 8, warmest SSTA is building in the central Pacific between 160°E and 140°W. Westerlies to the west and easterlies to the east converge into this warm region (Figure 5c) near the dateline. A weak upwelling Kelvin wave (Figure 6a dashed line) is initiated that is associated with these easterlies east of the dateline. At this time, the prevailing eastward flow is interrupted and westward currents are found in the eastern Pacific between months 6-8 (Figure 5d). The SSTA in the NINO3 region briefly cools (Figure 5a) in month 7. At this same time (forecast months 6-8), westerlies prevail from the western boundary all the way to the dateline. The next downwelling Kelvin wave is initiated in the west and arrives at the eastern boundary roughly at forecast month 9. As it enters the NINO3 region this downwelling Kelvin wave warms the SSTA. The warmest SSTA fills in to the west and by month 10 some of the warmest SSTA is located just east of the dateline. Bjerknes feedback becomes entrenched and westerlies to the west of the SSTA maximum converge with easterlies to the east (Figure 5c).

Careful examination of the equatorial signal and Kelvin/Rossby wave decomposition of the ocean waves helps to explain the timing and sign of the differences in the mean state in

Figure 4a. After 3 month forecasts, downwelling Kelvin waves that are forced by westerlies in the western Pacific, start to warm the eastern Pacific. After 7 month lead times, the Bjerknes feedback mechanism begins to lock in leading to enhanced westerlies over the western Pacific (Figure 5c) and growth of the air-sea coupled mode. The atmospheric impact of including the interannual forcing in the IO is to impart a large-scale downwelling favorable signal in the Pacific, increasing the warming in the NINO3 region after the 3 months. By 7 month lead times, the El Niño signal is enhanced/reinforced due to Bjerknes feedback.

To a large part, the previous discussion reinforces the conjecture of [*Annamalai et al.*, 2010] who suggested that the impact of the IO would be to enhance the westerlies along the equator and amplify an ongoing El Niño. However, examination of the various fields besides equatorial Hovmöller plots suggests that the initialization and growth of the warming in the NINO3 region is influenced by off-equatorial factors and by not only zonal but also meridional wind stress. Therefore, the discussion will now focus on the Pacific basin using plots of the mean forecast for 3, 5, 7, and 10 month lead times for SSTA, sea level anomaly, curl and divergence differences for INT_PAC, INT_IO minus INT_PAC, CLIM_IO results (Figure 7 to Figure 10, respectively).

On the equator, Ekman pumping velocity is undefined (since the Coriolis parameter is in the denominator). However, near the equator the wind stress divergence can be diagnosed to infer regions of upwelling or downwelling. By month 3 of the mean forecast, divergence corresponds to upwelling between 140^{o}E-150^{o}W on the equator and convergence is found between 140^{o}W-110^{o}W (Figure 7d). Off the equator, downwelling favorable curl (curl <0 in the Northern Hemisphere and > 0 in the Southern Hemisphere) can be seen west of 140^{o}W generally within 10^o of the equator (Figure 7c). West of 160^{o}W in the far western Pacific downwelling favorable curl off the equator corresponds to positive sea level anomalies off New Guinea (Figure 7b). This feature is important since it initiates the transition from the upwelling prior to month 3 across the basin to overall downwelling after that time. In other words, the off-equatorial curl initializes a downwelling Rossby wave and positive sea level anomaly in the far western Pacific that soon reflects as a downwelling Kelvin wave that begins the eventual transition to warm SSTA in the NINO3 region by month 7. This is an instance where the off-equatorial signal (a downwelling Rossby wave) contributes to converting upwelling to downwelling along the equator and so features prominently in ENSO predictability. Unfortunately, this downwelling in the west is not well represented by the Kelvin/Rossby decomposition plot (Figure 6) since it lies west of 160^{o}E which is the western extent of the land-free symmetric box that is required by this decomposition analysis. However, the subsequent downwelling Kelvin wave (spawned from the reflected Rossby wave) in the far west starting in month 4 is well diagnosed.

To the east, a pair of upwelling-favorable (negative in the Northern Hemisphere positive in the Southern Hemisphere) curl patches are located within 15^{o}S-10^{o}N between 140^{o}W-110^{o}W (Figure 7c). This feature corresponds with a pair of negative sea level anomalies centered at 5^{o}N and 12^{o}S at 130^{o}W and is identified as an upwelling Rossby wave in the Kelvin/Rossby diagnosis in Figure 6b. East of 160^{o}W, an upwelling Rossby wave at 140^{o}W acts to shoal the thermocline at 5^{o}N and 10^{o}S reshaping the meridional gradient to help focus the downwelling Kelvin wave train along the equator coming later in the average forecast.

In summary, downwelling Rossby waves forced by wind stress curl off the equator in the far western Pacific reflect to downwelling Kelvin waves eventually transitioning the NINO3 region to warming. The upwelling Rossby wave at 140^{o}W at month 3 shapes the meridional gradient to focus intensification on the equator.

By month 5 the downwelling Rossby wave hitting the western boundary in month 3 has reflected into a downwelling Kelvin wave and this wave has propagated eastward across the Pacific as far as ~140^{o}W (Figure 8b and Figure 6a). The effects of this downwelling Kelvin wave are demonstrated by positive sea level and SST anomaly throughout the waveguide (+/- 2^o) across the entire Pacific (Figure 8a). The upwelling features in Figure 8c are echoed in negative sea level at 5^{o}N and 10^{o}S at 145^{o}W (Figure 8b). The NINO3 region is warming and SSTA is largest at about 120^{o}W on the equator. It is also interesting to note that the warmest SSTA is just south of the equator whereas the sea level anomaly maximum is centered on the equator. Convergence found on the equator and positive curl and downwelling just to the south (5^{o}S-0^{o}S, 140^{o}W-110^{o}W) coincide with maximum SSTA. Going from 5^{o}N to 12^{o}S along 130^{o}W winds are starting northerly recurving to northwesterlies just south of the equator. West of the dateline and south of 5^{o}S, pervasive positive curl (downwelling favorable) is collocated with positive sea level anomaly against New Guinea and Australia coasts. To the north of the equator, positive curl and upwelling are found with negative sea level west of 150^{o}E off the Philippines. Thus the southeasterlies to the south recurving to southwesterlies north of the equator in the far western Pacific act to deepen and shoal sea level, respectively. To reiterate, not only are the equatorial signals important for the diagnosing the impact of the IO on ENSO, but the off-equatorial impacts such as oceanic Rossby wave formation and propagation are also important.

By month 7 the second Kelvin wave has reflected at the eastern boundary as a downwelling Rossby wave as evident by positive sea level at 10^{o}N, 5^{o}S at 120^{o}W (Figure 9b and Figure 6b). Another positive sea level and SSTA maximum is centered on the equator at

~170^{o}W (Figure 9a, b). Equatorial westerlies, best demonstrated by the westerly wind burst in Figure 5c that extends from the western boundary to 160^{o}E (note the 2x10^{-3} N/m^2 contour), force this downwelling Kelvin wave. To the north, downwelling curl corresponds to positive sea level and to the south negative sea level is collocated with upwelling favorable wind stress curl at 10^{o}N, 10^{o}S at ~150^{o}W, respectively. Off the equator, west of 160^{o}E the curl is positive to the north and this forces upwelling 0-10^{o}N and negative sea level. It is also interesting to note that upwelling curl within 5^o of the equator in the NINO3 region (particularly at 120^{o}W) is causing weak upwelling and cold SSTA at 5^{o}N driving the warmest SST south of the equator (Figure 9a).

By month 10 the Bjerknes feedback has locked in (Figure 10). SSTA is positive throughout the equatorial band between 160^{o}E to the eastern boundary. The negative sea level horseshoe pattern is evident off the equator in the west and positive values east of 160^{o}E near the equator typically associated with a mature El Niño. On the equator, winds are diverging between 150^{o}E-175^{o}E and converging to the east of there between 150^{o}W-100^{o}W. To the east of 150^{o}W and off the equator, the curl and sea level are in good agreement. At 10^{o}N, 150^{o}W, downwelling curl corresponds with positive sea level anomaly. At 2^{o}N, 135^{o}W positive curl overlays with a small region of negative sea level. Just south of the equator at 135^{o}W, downwelling curl coincides with a maximum of sea level and SSTA. Further to the south at 10^{o}S and 140^{o}W upwelling curl and negative sea level coincide. Thus the pattern of upwelling/downwelling curl of the wind maintains the meridional sea level gradient east of 160^{o}W. Off the equator west of 160^{o}W, upwelling curl is acting to reinforce the negative sea level off the Philippines and off the coast of New Guinea and Australia. To summarize, the mean forecast by 10 month lead times shows winds that are primarily diverging away from the equator west of the dateline (southwesterlies to the north and northwesterlies to the south of the equator) and converging towards the equator east of the dateline (with northeasterlies north of the equator slowing and turning towards northwesterlies at the equator). These diagnostics of the average coupled forecast reveals that the response of the ENSO system in the Pacific is more complicated than simply triggering a westerly wind burst in the western Pacific on the equator and setting off downwelling Kelvin waves eventually warming the NINO3 region as assumed by [*Annamalai et al.*, 2010] and others. Our diagnosis suggests that the atmospheric response is more complicated than previously thought, and a previously unaccounted-for significant signal corresponds to strong easterlies south of 15^{o}S and between 0^{o}N to 20^{o}N.

Our results may be usefully contrasted with previous work employing simpler atmospheric models and idealized surface forcing. Similar to previous work, there are weak westerlies near the equator (10^{o}S-0^{o}N) across the entire Pacific. These relatively weak winds we simulate near the equator match those of [*Annamalai et al.*, 2005] who used a simple linear atmospheric model (a moist linear baroclinic model – LBM of [*Watanabe and Jin*, 2003]) to show that the atmospheric Kelvin wave of the western dipole of the IODZM cancels that of the eastern dipole (their Figures 8b, 10d). However, our results show the importance of not only the near-equatorial winds but also the off-equatorial zonal and meridional winds for the diagnosis of the IO SSTA teleconnections to Pacific ENSO (Figure 2a).

The off-equatorial easterlies represented in Figure 2a are a prominent feature but are lacking in previous studies (e.g. [*Wu and Kirtman*, 2004] Figure 7d, [*Annamalai et al.*, 2010] Figure 7d). There are several reasons why the simple atmospheric models that were used to highlight the IO atmospheric teleconnections to the Pacific ([*Wu and Kirtman*, 2004] and [*Annamalai et al.*, 2010]) might lack the off-equatorial easterlies simulated in SPEEDY. In previous results, the IO SST field is idealized in some way or another. Either the 1st EOF of the coupled model results or the SST differences with and without IODZM for El Niño is utilized to simplify the SST forcing. In addition, these models have been linearized about different mean states for specific seasons (JJAS and MJ, respectively) so the seasonal cycle remaining in SPEEDY may play a role in forming the off-equatorial easterlies. When we limit the SSTA forcing in the IO to just the 1st EOF of the simulated SSTA (not shown but a similar pattern as [*Wu and Kirtman*, 2004] Figure 7a for the IO) for the forced SPEEDY AGCM, the anomalous westerlies near the equator are enhanced: the atmospheric Kelvin wave is present as in previous research but the easterlies off the equator remain.

The lack of a strong signal off the equator for the LBM results of the previous authors is surprising considering the results of [*Watanabe and Jin*, 2003]. They used a similar model (LBM) as previous authors and forced it with El Niño minus La Niña observed SSTA limited to the IO region. Their Figure 8c indicates that a basin-scale cooling in the IO (their M3 region) results in a positive precipitation response symmetric within 15^{o} of the equator that is centered at 140^{o}E. West of the dateline, the 850 mb streamfunction response to this heating shows nearly collocated cyclonic flow and easterlies between 10^{o}N-35^{o}N, westerlies for 5^{o}N-10^{o}S, and easterlies between 15^{o}S-30^{o}S west of the dateline, which are broadly similar to our results. On the other hand, our precipitation results have this maximum centered to the east, at roughly 160^{o}W (Figure 2c), so this displacement of the precipitation heating might explain the elongated off-equatorial easterlies found in the SPEEDY results (Figure 2a).

Another potential difference between previously reported results and the current wind results is the amplitude and location of the precipitation anomalies in the Pacific. For example, [*Annamalai et al.*, 2010] shows (their Figure 2b) the strong positive precipitation anomalies centered at 10^{o}S and 5^{o}N centered at 180^{o}, roughly similar to our results. However, for these previous results there is also a strong negative anomaly with similar zonal extent and amplitude to the west, centered at 150^{o}E that may act to offset any off-equatorial signal in the winds. Our precipitation results (Figure 2c) show that there are no such offsetting precipitation anomalies to the west of the main positive values located between 160^{o}E to 160^{o}W centered at 10^{o}S and 5^{o}N. Therefore, off-equatorial easterlies are not opposed by westerlies for the SPEEDY results.

The last and most likely potential reason for off-equatorial easterlies may be the convective scheme within the SPEEDY results. [*Kim et al.*, 2008] show that implementation of CMT leads to enhanced off-equatorial precipitation (roughly 5^{o}-15^{o} off the equator) and decreased precipitation between 5^{o}S-5^{o}N. The wind response to implementation of CMT is increased 850 mb westerlies between 10^{o}S-10^{o}N and also easterlies poleward of the enhanced precipitation. However, these results are only valid west of 150^{o}W for the December - February climatological forcing used for the [*Kim et al.*, 2008] example. A fundamental concept of CMT is that upper atmosphere momentum is transported to the surface via downdrafts around convection. In our example, the generally enhanced precipitation (Figure 2c) between 15^{o}S-5^{o}N drags westerly momentum from upper branch of the Walker circulation to the surface (Figure 2a). At the same time, weaker precipitation for the coupled IO with respect to the decoupled IO does the opposite leaving enhanced easterlies between 5^{o}N-20^{o}N and south of 15^{o}S. Thus, implementation of CMT within SPEEDY, but not within any of the linear model results, may also contribute to the off-equatorial easterlies found in the SPEEDY results. Although there are multiple potential reasons for differences between the nonlinear LBM and SPEEDY atmospheric results, exploring differences further is beyond the scope of the current paper.

The combined impact of the zonal and meridional winds in the Pacific on the ocean can be conveniently summarized by diagnosing the differences of the SPEEDY experiments using curl and divergence of the wind stress. On the equator, surface convergence of the wind leads to convergence of the surface currents, downwelling in the ocean, a deepening of the thermocline, and an increase in sea level. The divergence of the atmospheric teleconnections is presented in Figure 2f and this shows pervasive downwelling favorable winds all along the entire equator. Off the equator, the curl can be used to estimate the sense of Ekman pumping velocity as a measure of upwelling or downwelling. Figure 2e shows that upwelling favorable winds (positive in the Northern Hemisphere and negative in the Southern Hemisphere) are predominant between 15^{o}S to 10^{o}N in the Pacific. However, the curl just to the south of the equator between 160^{o}E-140^{o}W is positive indicating a narrow band of downwelling favorable curl. North of ~10^{o}N and in the southwest Pacific (off Australia) downwelling curl is also prevalent.

To summarize differences between the present study and prior work, forced experimental minus control atmospheric simulations produce strong easterly differences south of 15^{o}S and between the equator and 20^{o}N in the Pacific, with weak westerly differences near the equator between 10^{o}S and the equator. For the meridional component, winds converge towards 5^{o}S especially over the eastern half of the basin with abundant precipitation in the eastern Pacific cold tongue region near the equator. In addition, differences show strong positive precipitation anomalies in the central Pacific. Convergence along the equator indicates that there is pervasive downwelling favorable conditions present at initialization of the coupled system along the equator. However, off the equator between 15^{o}S-10^{o}N the prevailing curl indicates that IO SSTA is generally forcing upwelling in this region. As [*Annamalai et al.*, 2005] noted, the weak winds within the waveguide may allow nascent El Niño/La Niña events to grow unencumbered.

6 Summary and Conclusions

Our results suggest that additional validated forecast skill is available for operational ENSO forecasting improvements by including IO forcing and realistically nonlinear modelling of the response of the coupled Indo-Pacific ocean atmosphere system. A key potential source that we have identified in this study is the impact of atmospheric teleconnections originating from the IO. Coupled experiments described herein that are initialized with the full observed SST forcing and utilize a nonlinear atmosphere indicate that our atmospheric response in the Pacific to interannual IO forcing includes weak westerly winds equatorward of 10^{o}S, enhanced off-equatorial trade winds and strengthened easterlies between 30^{o}S to 15^{o}S and the equator to 25^{o}N. The differences between the previous linear atmospheric model and our AGCM (SPEEDY) results may be due to either simplification of IO forcing, displacement of precipitation (and heating) to the east with no compensating anomaly, or most likely, the convective momentum transport in SPEEDY. These off-equatorial winds have profound impact in that they generate wind stress curl that act to amplify the oceanic Rossby wave signal which eventually impact the eastern Pacific by way of reflected Kelvin waves.

Differences between coupled experiments show that including the impact of interannual teleconnections from the IO have significantly higher ENSO correlation (exceeding the 95% significance level from 3-9 months) and lower RMS validation statistics. The reason for this is a combination of equatorial and off-equatorial coupling that eventually warms the NINO3 region. Early in the forecast period, prior to 3 month lead times, equatorial upwelling in the western Pacific weakly cools the NINO3 region via propagation of upwelling Kelvin waves. After that time, off-equatorial downwelling favorable curl in the western Pacific helps to amplify the transition from cooling to warming in the NINO3 region by way of reflected downwelling Rossby to downwelling Kelvin waves. Downwelling Kelvin waves, amplified by equatorial convergence, warm the eastern Pacific and improve correlation validation after 3 month lead times with respect to observations. The improvement in correlation peaks at 7 months which corresponds with the time it takes for the transmission of the reflected downwelling Rossby wave to reflect into the downwelling Kelvin wave then to propagate across the Pacific into the NINO3 region. Therefore, a main conclusion from these results is that the interannual variability of IO SST forcing is responsible for overall somewhat lagged widespread downwelling in the Pacific, assisted by off-equatorial curl, leading to warmer NINO3 SST anomaly and improved validation after 3 month lead times.

Currently ENSO forecast discussions (see http://origin.cpc.ncep.noaa.gov/products/GODAS/ocean_briefing_gif/global_ocean_monitoring_current.ppt) include descriptions of large-scale ocean waves present in the initialization of coupled forecasts. However, these discussions only assess the state of the oceanic Kelvin wave (using the Ocean Kelvin Wave Index, an extended EOF technique) and this would suggest a lack of emphasis on off-equatorial processes in coupled model initialization. On the contrary, the results of the impact of the teleconnections from the IO to the Pacific presented herein demonstrate the significance of the off-equatorial processes that generate oceanic Rossby waves. Therefore, we recommend that the impact of the Rossby waves on ENSO should be included in forecast discussions. We have shown that the impact of the IO atmospheric teleconnections to ENSO significantly improve coupled forecasts from 3-9 month lead times, so both upstream IO influences and off-equatorial processes should be considered/included in ENSO forecasting systems.

Acknowledgments

This work was completed as part of the Accomplished Scientist Ph. D. Program at the University of Maryland. We would like to thank Dr. Fred Kucharski who provided all software and guidance on implementing SPEEDY into our coupled model. The SPEEDY model is freely available and can be downloaded from http://users.ictp.it/~kucharsk/speedy-net.html. Dr. Travis Sluka helped with early questions about CMT and SPEEDY and Dr. Hugo Berbery provided his expertise on atmospheric model questions. We gratefully acknowledge the comments from the anonymous reviewers who helped to improve this manuscript. We acknowledge NASA for supporting much of the research contained in this paper (NASA Grants NNX13AM61G, NNX09AF41G, and NNX16AH62G). We would also thank everyone involved with development of the ocean model particularly James Beauchamp and Joaquim Ballabrera-Poy. The source code for the ocean model used in this study is freely available. Both the data and input files necessary to reproduce the experiments with our OGCM are available from the authors upon request (ehackert@essic.umd.edu). All observational data for this paper is properly cited and referred to in the reference list.

References

Adler, R. F., et al. (2003), The version-2 global precipitation climatology project (GPCP) monthly precipitation analysis (1979-present), *Journal of Hydrometeorology*, *4*(6), 1147-1167.

Alexander, M. A., I. Blade, M. Newman, J. R. Lanzante, N. C. Lau, and J. D. Scott (2002), The atmospheric bridge: The influence of ENSO teleconnections on air-sea interaction over the global oceans, *Journal of Climate*, *15*(16), 2205-2231.

Annamalai, H., S. Kida, and J. Hafner (2010), Potential Impact of the Tropical Indian Ocean-Indonesian Seas on El Nino Characteristics, *Journal of Climate*, *23*(14), 3933-3952.

Annamalai, H., S. P. Xie, J. P. McCreary, and R. Murtugudde (2005), Impact of Indian Ocean sea surface temperature on developing El Niño, *Journal of Climate*, *18*(2), 302-319.

Antonov, J. I., D. Seidov, T. P. Boyer, R. A. Locarnini, A. V. Mishonov, H. E. Garcia, O. K. Baranova, M. M. Zweng, and D. R. Johnson (2010), World Ocean Atlas 2009, Volume 2: Salinity., in *NOAA Atlas NESDIS 69*, edited by Secondary Antonov, J. I., D. Seidov, T. P. Boyer, R. A. Locarnini, A. V. Mishonov, H. E. Garcia, O. K. Baranova, M. M. Zweng, and D. R. Johnson, p. 184 pp., U.S. Government Printing Office, Washington, D.C.

Behringer, D. (2007), The Global Ocean Data Assimilation System (GODAS) at NCEP, paper presented at 11th Symp. on Integrated Observing and Assimilation Systems for Atmosphere, Oceans and Land Surface, American Meteorological Society San Antonio, TX [Available online at http://ams.confex.com/ams/pdfpapers/119541.pdf].

Bracco, A., F. Kucharski, F. Molteni, W. Hazeleger, and C. Severijns (2005), Internal and forced modes of variability in the Indian Ocean, *Geophysical Research Letters*, *32*(12).

Chen, D., L. M. Rothstein, and A. J. Busalacchi (1994), A Hybrid Vertical Mixing Scheme and Its Application to Tropical Ocean Models, *Journal of Physical Oceanography*, *24*(10), 2156-2179.

Delcroix, T., J. P. Boulanger, F. Masia, and C. Menkes (1994), Geosat-Derived Sea-Level and Surface Current Anomalies in the Equatorial Pacific During the 1986-1989 El-Niño and La-Niña, *Journal of Geophysical Research-Oceans*, *99*(C12), 25093-25107.

ECMWF (1994), The description of the ECMWF/WCRP Level III-A Global Atmospheric Data Archive, *Tech. Attach.Rep.*, 72 pp. pp, European Centre for Medium-Range Weather Forecasts, Reading, England, U.K.

Gent, P. R., and M. A. Cane (1989), A Reduced Gravity, Primitive Equation Model of the Upper Equatorial Ocean, *Journal of Computational Physics*, *81*(2), 444-480.

Gibson, J. K., P. Kallberg, S. Uppala, F. Hernandez, R. Nomura, and Y. Serrano (1997), ECMWF re-analysis. *Rep.*, European Centre for Medium-Range Weather Forecasts, Reading (UK).

Glantz, M. H. (2001), *Currents of Change: El Nino and La Nina Impacts on Climate and Society*, 252 pp., Cambridge University Press, Cambridge, UK.

Griffies, S. M., M. J. Harrison, R. C. Pacanowski, and A. Rosati (2004), Techical Guide to MOM4, in *GFDL Ocean Group Technical Report 5* edited by Secondary Griffies, S. M., M. J. Harrison, R. C. Pacanowski, and A. Rosati, p. 337, GFDL GFDL Princeton, NJ [Available online at www.gfdl.noaa.gov/~fms].

Hackert, E., A. Busalacchi, and J. Ballabrera-Poy (2014), Impact of Aquarius sea surface salinity observations on coupled forecasts for the tropical Indo-Pacific Ocean, *Journal of Geophysical Research, Oceans*, *119*(doi: 10.1002/2013JC009697).

Hackert, E., J. Ballabrera-Poy, A. J. Busalacchi, R. H. Zhang, and R. Murtugudde (2007), Comparison between 1997 and 2002 El Nino events: Role of initial state versus forcing, *Journal of Geophysical Research-Oceans*, *112*(C1).

Hackert, E. C., A. J. Busalacchi, and R. Murtugudde (2001), A wind comparison study using an ocean general circulation model for the 1999-1998 El Niño, *Journal of Geophysical Research-Oceans*, *106*(C2), 2345-2362.

Horel, J. D., and J. M. Wallace (1981), PLANETARY-SCALE ATMOSPHERIC PHENOMENA ASSOCIATED WITH THE SOUTHERN OSCILLATION, *Monthly Weather Review*, *109*(4), 813-829.

Huang, R. X. (1993), Real Fresh-Water Flux as a Natural Boundary-Condition for the Salinity Balance and Thermohaline Circulation Forced by Evaporation and Precipitation, *Journal of Physical Oceanography*, *23*(11), 2428-2446.

Kalnay, E., et al. (1996), The NCEP/NCAR 40-year reanalysis project, *Bulletin of the American Meteorological Society*, *77*(3), 437-471.

Kessler, W. S., M. J. McPhaden, and K. M. Weickmann (1995), Forcing of Intraseasonal Kelvin Waves in the Equatorial Pacific, *Journal of Geophysical Research-Oceans*, *100*(C6), 10613-10631.

Kim, D., J. S. Kug, I. S. Kang, F. F. Jin, and A. T. Wittenberg (2008), Tropical Pacific impacts of convective momentum transport in the SNU coupled GCM, *Climate Dynamics*, *31*(2-3), 213-226.

Kraus, E. B., and J. S. Turner (1967), A One-Dimensional Model of Seasonal Thermocline .2. General Theory and Its Consequences, *Tellus*, *19*(1), 98-&.

Kroeger, J., and F. Kucharski (2011), Sensitivity of ENSO characteristics to a new interactive flux correction scheme in a coupled GCM, *Climate Dynamics*, *36*(1-2), 119-137.

Kucharski, F., F. Molteni, and J. H. Yoo (2006), SST forcing of decadal Indian Monsoon rainfall variability, *Geophysical Research Letters*, *33*(3).

Kucharski, F., I. S. Kang, R. Farneti, and L. Feudale (2011), Tropical Pacific response to 20th century Atlantic warming, *Geophysical Research Letters*, *38*.

Kucharski, F., F. Molteni, M. P. King, R. Farneti, I.-S. Kang, and L. Feudale (2013), On the Need of Intermediate Complexity General Circulation Models A "SPEEDY" Example, *Bulletin of the American Meteorological Society*, *94*(1), 25-30.

Lau, N. C., and M. J. Nath (2003), Atmosphere-ocean variations in the Indo-Pacific sector during ENSO episodes, *Journal of Climate*, *16*(1), 3-20.

Locarnini, R. A., A. V. Mishonov, J. I. Antonov, T. P. Boyer, H. E. Garcia, O. K. Baranova, M. M. Zweng, and D. R. Johnson (2010), World Ocean Atlas 2009, Volume 1: Temperature, NOAA Atlas NESDIS 68, edited by Secondary Locarnini, R. A., A. V. Mishonov, J. I. Antonov, T. P. Boyer, H. E. Garcia, O. K. Baranova, M. M. Zweng, and D. R. Johnson, p. 184 pp., U.S. Government Printing Office, Washington, D.C.

McPhaden, M. J. (2015), Playing hide and seek with El Nino, *Nature Clim. Change*, *5*(9), 791-795.

Menkes, C. E., M. Lengaigne, J. Vialard, M. Puy, P. Marchesiello, S. Cravatte, and G. Cambon (2014), About the role of Westerly Wind Events in the possible development of an El Nino in 2014, *Geophysical Research Letters*, *41*(18), 6476-6483.

Min, Q., J. Su, R. Zhang, and X. Rong (2015), What hindered the El Nino pattern in 2014?, *Geophysical Research Letters*, *42*(16), 6762-6770.

Molteni, F. (2003), Atmospheric simulations using a GCM with simplified physical parametrizations. I: model climatology and variability in multi-decadal experiments, *Climate Dynamics*, *20*(2-3), 175-191.

Murtugudde, R., and A. J. Busalacchi (1998), Salinity effects in a tropical ocean model, *Journal of Geophysical Research-Oceans*, *103*(C2), 3283-3300.

Murtugudde, R., R. Seager, and A. Busalacchi (1996), Simulation of the tropical oceans with an ocean GCM coupled to an atmospheric mixed-layer model, *Journal of Climate*, *9*(8), 1795-1815.

Murtugudde, R., A. J. Busalacchi, and J. Beauchamp (1998), Seasonal-to-interannual effects of the Indonesian Throughflow on the tropical Indo-Pacific Basin, *Journal of Geophysical Research-Oceans*, *103*(C10), 21425-21441.

National Academies of Sciences, E., and Medicine (2016), *Next Generation Earth System Prediction: Strategies for Subseasonal to Seasonal Forecasts*, 290 pp., The National Academies Press, Washington, DC.

National Research Council (2010), *Assessment of intraseasonal to interannual climate prediction and predictability*, National Academies Press, Washington, D.C. :.

Picaut, J., and R. Tournier (1991), MONITORING THE 1979-1985 EQUATORIAL PACIFIC CURRENT TRANSPORTS WITH EXPENDABLE BATHYTHERMOGRAPH DATA, *Journal of Geophysical Research: Planets*, *96*, 3263-3277.

Price, J. F., R. A. Weller, and R. Pinkel (1986), Diurnal Cycling - Observations and Models of the Upper Ocean Response to Diurnal Heating, Cooling, and Wind Mixing, *Journal of Geophysical Research-Oceans*, *91*(C7), 8411-8427.

Quenouille, M. H. (1952), *Associated measurements*, 242 pp., Buterworths, London.

Rayner, N. A., D. E. Parker, E. B. Horton, C. K. Folland, L. V. Alexander, D. P. Rowell, E. C. Kent, and A. Kaplan (2003), Global analyses of sea surface temperature, sea ice, and night marine air temperature since the late nineteenth century, *Journal of Geophysical Research-Atmospheres*, *108*(D14).

Reynolds, R. W., N. A. Rayner, T. M. Smith, D. C. Stokes, and W. Q. Wang (2002), An improved in situ and satellite SST analysis for climate, *Journal of Climate*, *15*(13), 1609-1625.

Rossow, W. B., and R. A. Schiffer (1991), Isccp Cloud Data Products, *Bulletin of the American Meteorological Society*, *72*(1), 2-20.

Saha, S., et al. (2014), The NCEP Climate Forecast System Version 2, *Journal of Climate*, *27*(6), 2185-2208.

Saha, S., et al. (2010), THE NCEP CLIMATE FORECAST SYSTEM REANALYSIS, *Bulletin of the American Meteorological Society*, *91*(8), 1015-1057.

Santoso, A., M. H. England, and W. Cai (2012), Impact of Indo-Pacific Feedback Interactions on ENSO Dynamics Diagnosed Using Ensemble Climate Simulations, *Journal of Climate*, *25*(21), 7743-7763.

Steiger, J. H. (1980), TESTS FOR COMPARING ELEMENTS OF A CORRELATION MATRIX, *Psychological Bulletin*, *87*(2), 245-251.

Uehara, H., A. A. Kruts, H. Mitsudera, T. Nakamura, Y. N. Volkov, and M. Wakatsuchi (2014), Remotely propagating salinity anomaly varies the source of North Pacific ventilation, *Progress in Oceanography*, *126*, 80-97.

Watanabe, M., and F. F. Jin (2003), A moist linear baroclinic model: Coupled dynamical-convective response to El Nino, *Journal of Climate*, *16*(8), 1121-1139.

Wu, R. G., and B. P. Kirtman (2004), Understanding the impacts of the Indian Ocean on ENSO variability in a coupled GCM, *Journal of Climate*, *17*(20), 4019-4031.

Xie, P. P., and P. A. Arkin (1998), Global monthly precipitation estimates from satellite-observed outgoing longwave radiation, *Journal of Climate*, *11*(2), 137-164.

Yu, J. Y., C. R. Mechoso, J. C. McWilliams, and A. Arakawa (2002), Impacts of the Indian Ocean on the ENSO cycle, *Geophysical Research Letters*, *29*(8).

Zhou, L., R. B. Neale, M. Jochum, and R. Murtugudde (2012), Improved Madden-Julian Oscillations with Improved Physics: The Impact of Modified Convection Parameterizations, *Journal of Climate*, *25*(4), 1116-1136.

Figure 1: Validation of the SPEEDY coupled model. Our Indo-Pacific SPEEDY coupled model (red) is a) correlated and b) RMSD against observed NINO3 SSTA for Jan. 1993-Mar. 2011. CFSRR coupled model results (black) are included to put our coupled results into the context of a more widely known coupled model. Individual correlations exceed the 95% significance out to 8.3 (35) and 10 months (34) (effective degrees of freedom) for red and black lines, respectively. Observation persistence is indicated by the thin black dotted line. This version of the SPEEDY coupled model assimilates all available satellite (sea level, SST) and in situ information (sea surface salinity and subsurface temperature and salinity) using the data assimilation technique described in [*Hackert et al.*, 2014].

Figure 2: Impact of interannual IO SST forcing. Differences between two sets of SPEEDY atmosphere-only experiments for a) zonal, b) meridional wind stress, c) precipitation, d) vector representation of a) and b), e) curl and f) divergence of the wind stress. Differences are full SST anomaly forcing over the Indo-Pacific region (i.e. INT_PAC, INT_IO) minus the experiment that uses climatological seasonal cycle forcing over the IO (INT_PAC, CLIM_IO). Letters “U” and “D” represent regions of upwelling and downwelling favorable winds and absolute values greater than 3.3×10^{-3} N/m^2, 2.7×10^{-3} N/m^2, 13.2 mm/mon, 0.53×10^{-9} N/m^3, 0.35×10^{-9} N/m^3 are significant at the 95% level for a), b) c), e), and f), respectively.

Figure 3: Impact of IO interannual forcing on coupled NINO3 SST results. Validation statistics for a) correlation and b) RMS differences between coupled experiments with full atmospheric coupling (i.e. INT_PAC, INT_IO) in red and interannual coupling in the Pacific and climatological forcing in the IO (i.e. INT_PAC, CLIM_IO) in blue. The coupled experiments are validated against observed NINO3 SST anomaly for 1993 to 2014. Individual correlations exceed the 95% significance out to 8 (43) and 5.8 months (41) (effective degrees of freedom) for red and blue lines, respectively. The thick black line on the top x-axis shows where the red line is significantly larger than the blue line using the Steiger-Z test.

Figure 4: Mean and variability of NINO3 SST for impact of interannual IO SST forcing. Plots showing the NINO3 SST a) mean forecast and b) variability for INT_PAC, INT_IO (red) and INT_PAC, CLIM_IO (blue) for all forecasts from 1993-2014.

Figure 5: Hovmöller plots of impact of interannual IO SST forcing. Plots showing the mean temporal evolution of the impact of IO atmospheric coupling using longitude versus lead time (in months) averaged between 2^{o}N and 2^{o}S for a) SST, b) sea level (SL), c) zonal wind stress, and d) zonal currents. The mean is taken for the average forecast differences, INT_PAC, INT_IO minus INT_PAC, CLIM_IO, over all months from 1993 to 2014.

Figure 6: Kelvin/Rossby wave decomposition of interannual IO SST forcing. Longitude versus time distribution of the equatorial (a) Kelvin and (b) the first meridional mode of equatorial Rossby waves through their signature in zonal surface current deduced from the average forecast SL differences, (INT_PAC, INT_IO) – (INT_PAC, CLIM_IO). In order to follow possible wave reflections on the western (WB) and eastern (EB) boundaries, the Rossby panel (b) is inverted and the Kelvin wave pattern is repeated (c). The color scale for the Rossby panel is also inverted since reflection on meridional boundaries results in zonal currents of opposite sign. Solid lines (downwelling) and dashed lines (upwelling) represent theoretical wave speeds for Kelvin (2.5m/s) and Rossby waves (-0.8m/s or ~5months to cross this Pacific basin at 5^{o}N) on each plot.

Figure 7: Average 3 month forecast INT_PAC, INT_IO - INT_PAC, CLIM_IO. Average forecast values for month 3 for a) SST, b) sea level, c) curl of the wind stress (color) and wind stress (vector), and d) divergence of the wind stress (color) and wind stress (vector). The scale of the vector plot is indicated in the bottom left of the panel. For the reader's convenience, regions of upwelling and downwelling are marked by letters U and D, respectively.

Figure 8: Average 5 month forecast INT_PAC, INT_IO - INT_PAC, CLIM_IO. Same as previous but for 5 month average forecasts.

Figure 9: Average 7 month forecast INT_PAC, INT_IO - INT_PAC, CLIM_IO. Same as previous but for 7 month lead forecast mean.

Figure 10: Average 10 month forecast INT_PAC, INT_IO - INT_PAC, CLIM_IO. Same as previous but for 10 month forecast mean.

Experiment Name	Period	Model Geometry (Atmosphere/Ocean)	Indo-Pacific Forcing
INT_PAC, INT_IO	1993-2014	Global/Indo-Pacific	Interannual SSTA forcing for Pacific and IO
INT_PAC, CLIM_IO	1993-2014	Global/Indo-Pacific	Interannual SSTA forcing for Pacific, climatological seasonal cycle SST for IO

Table 1: Experiment description for impact of interannual IO SST forcing. The far left column describes the experiments, "INT" and "CLIM" stand for interannual and climatological forcing and "PAC" and "IO" stand for Pacific (30^{o}S-30^{o}N, 130^{o}E-70^{o}W) and Indian Oceans (30^{o}S-30^{o}N, 30^{o}E-129^{o}E), respectively. The far right column describes the SST anomaly forcing (SSTA) for the Indo-Pacific region. In order to isolate the impact of the IO, differences between INT_PAC, INT_IO – INT_PAC, CLIM_IO are presented. Note that SSTA are formulated with respect to the 1983-2014 mean seasonal cycle using [Reynolds et al., 2002] OI SST.

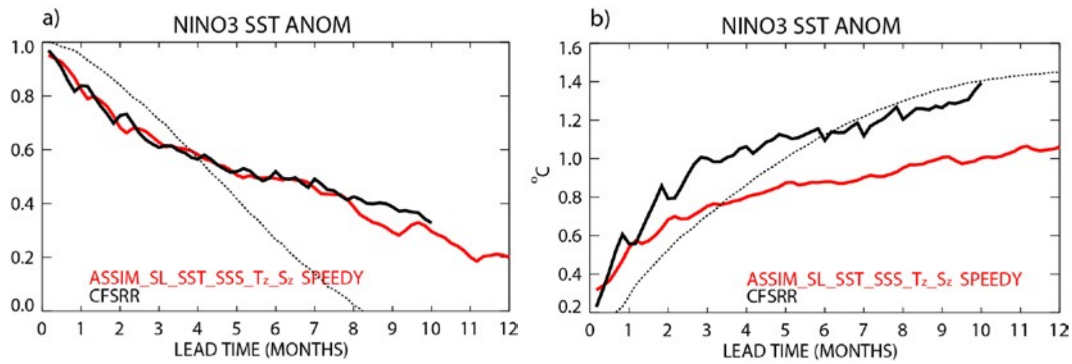

Figure 1: Validation of the SPEEDY coupled model. Our Indo-Pacific SPEEDY coupled model (red) is a) correlated and b) RMSD against observed NINO3 SSTA for Jan. 1993-Mar. 2011. CFSRR coupled model results (black) are included to put our coupled results into the context of a more widely known coupled model. Individual correlations exceed the 95% significance out to 8.3 (35) and 10 months (34) (effective degrees of freedom) for red and black lines, respectively. Observation persistence is indicated by the thin black dotted line. This version of the SPEEDY coupled model assimilates all available satellite (sea level, SST) and in situ information (sea surface salinity and subsurface temperature and salinity) using the data assimilation technique described in [*Hackert et al.*, 2014].

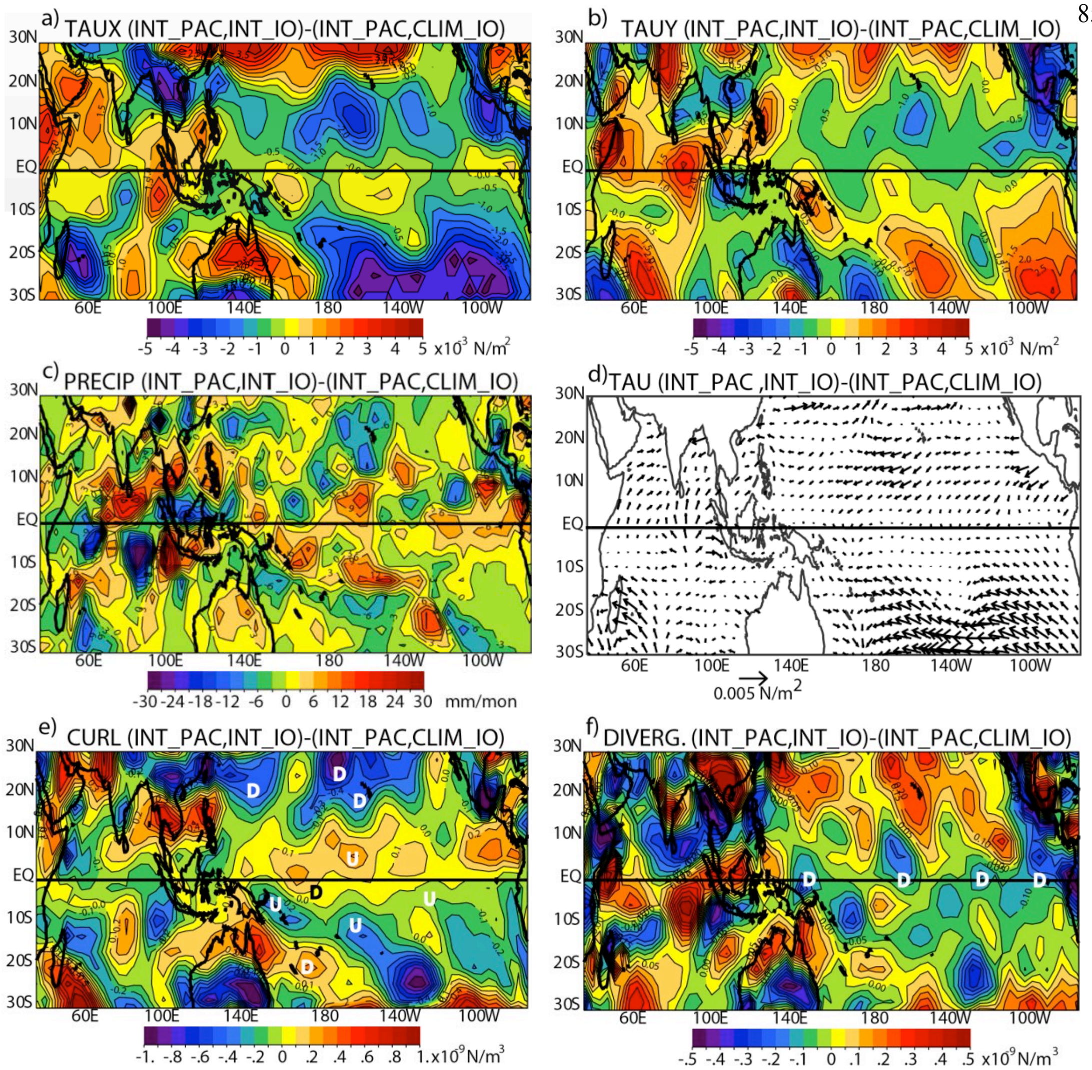

Figure 2: Impact of interannual IO SST forcing. Differences between two sets of SPEEDY atmospheric-only experiments for a) zonal, b) meridional wind stress, c) precipitation, d) vector representation of a) and b), e) curl and f) divergence of the wind stress. Differences are full SST anomaly forcing over the Indo-Pacific region (i.e. INT_PAC, INT_IO) minus the experiment that uses climatological seasonal cycle forcing over the IO (INT_PAC, CLIM_IO). Letters "U" and "D" represent regions of upwelling and downwelling favorable winds and absolute values greater than $3.3x10^{-3}$ N/m^2, $2.7x10^{-3}$ N/m^2, 13.2 mm/mon, $0.53x10^{-9}$ N/m^3, $0.35x10^{-9}$ N/m^3 are significant at the 95% level for a), b) c), e), and f), respectively.

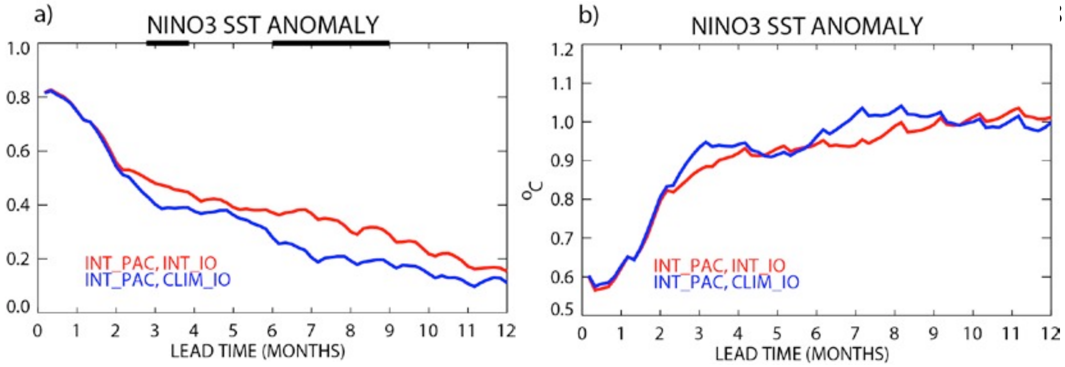

Figure 3: Impact of IO interannual forcing on coupled NINO3 SST results. Validation statistics for a) correlation and b) RMS differences between coupled experiments with full atmospheric coupling (i.e. INT_PAC, INT_IO in red and interannual coupling in the Pacific and climatological forcing in the IO (i.e. INT_PAC, CLIM_IO) in blue. The coupled experiments are validated against observed NINO3 SST anomaly for 1993 to 2014. Individual correlations exceed the 95% significance out to 8 (43) and 5.8 months (41) (effective degrees of freedom) for red and blue lines, respectively. The thick black line on the top x-axis shows where the red line is significantly larger than the blue line using the Steiger-Z test.

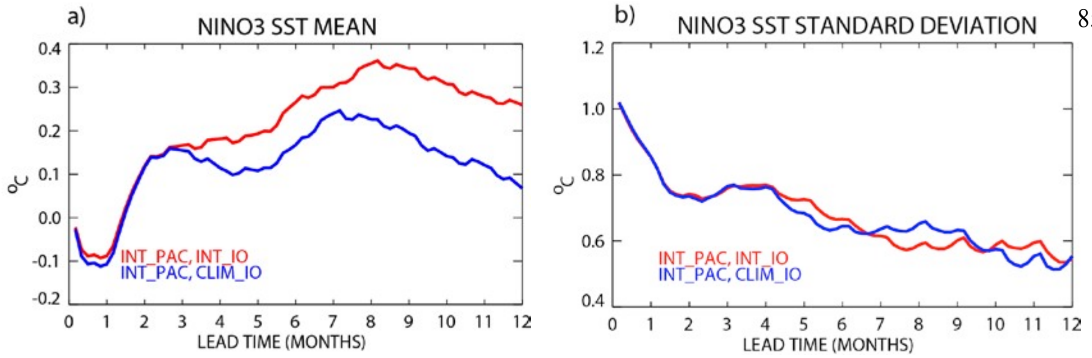

Figure 4: Mean and variability of NINO3 SST for impact of interannual IO SST forcing. Plots showing the NINO3 SST a) mean forecast and b) variability for INT_PAC, INT_IO (red) and INT_PAC, CLIM_IO (blue) for all forecasts from 1993-2014.

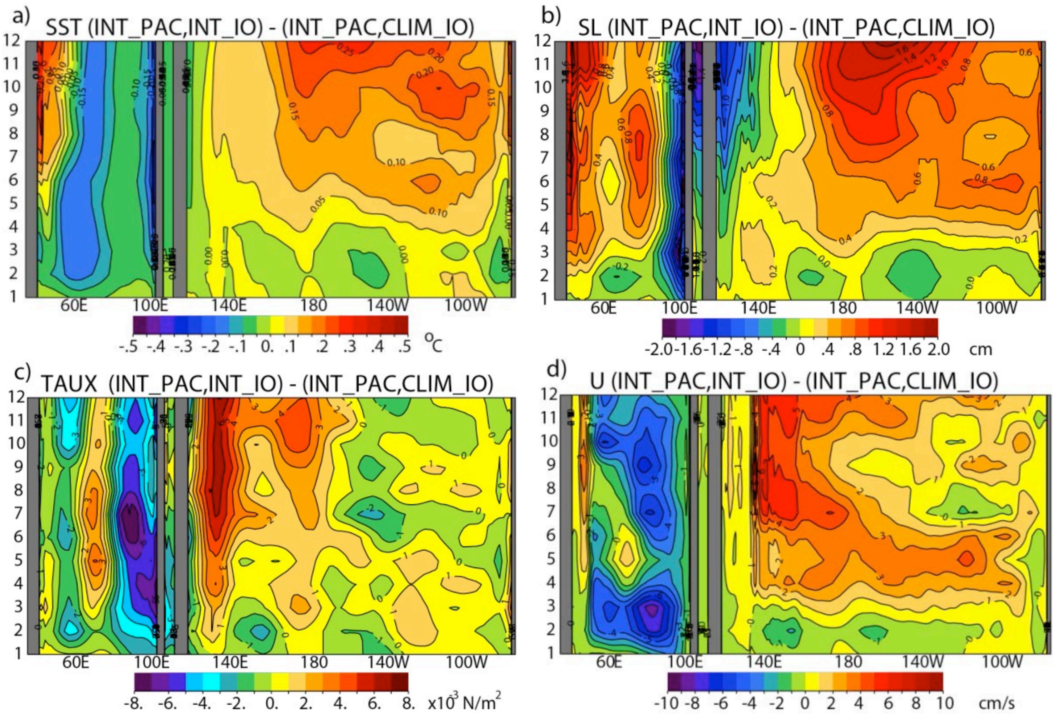

Figure 5: Hovmöller plots of impact of interannual IO SST forcing. Plots showing the mean temporal evolution of the impact of IO atmospheric coupling using longitude versus lead time (in months) averaged between 2^{o}N and 2^{o}S for a) SST, b) sea level (SL), c) zonal wind stress, and d) zonal currents. The mean is taken for the average forecast differences, INT_PAC, INT_IO minus INT_PAC, CLIM_IO, over all months from 1993 to 2014.

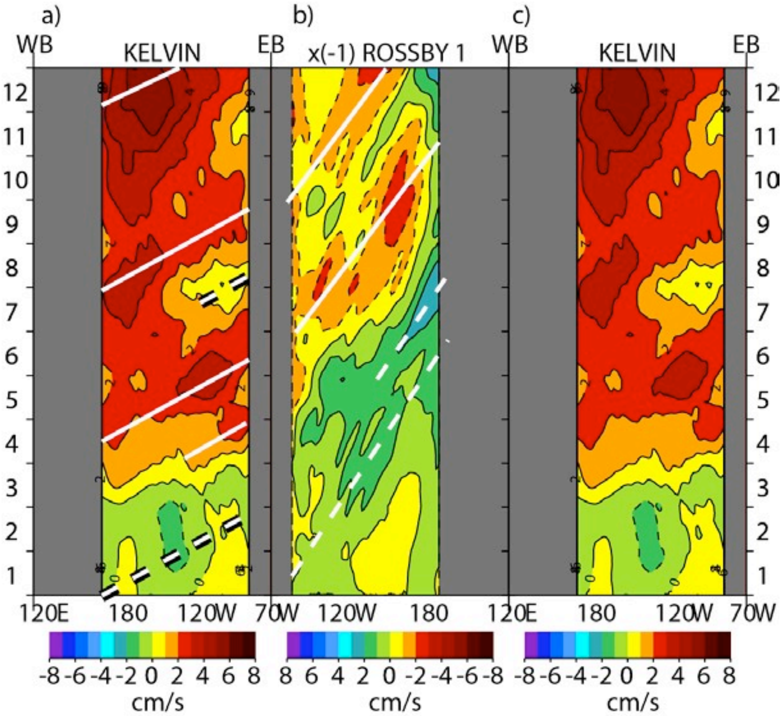

Figure 6: Kelvin/Rossby wave decomposition of interannual IO SST forcing. Longitude versus time distribution of the equatorial (a) Kelvin and (b) the first meridional mode of equatorial Rossby waves through their signature in zonal surface current deduced from the average forecast SL differences, (INT_PAC, INT_IO) – (INT_PAC, CLIM_IO). In order to follow possible wave reflections on the western (WB) and eastern (EB) boundaries, the Rossby panel (b) is inverted and the Kelvin wave pattern is repeated (c). The color scale for the Rossby panel is also inverted since reflection on meridional boundaries results in zonal currents of opposite sign. Solid lines (downwelling) and dashed lines (upwelling) represent theoretical wave speeds for Kelvin (2.5m/s) and Rossby waves (-0.8m/s or ~5months to cross this Pacific basin at 5^{o}N) on each plot.

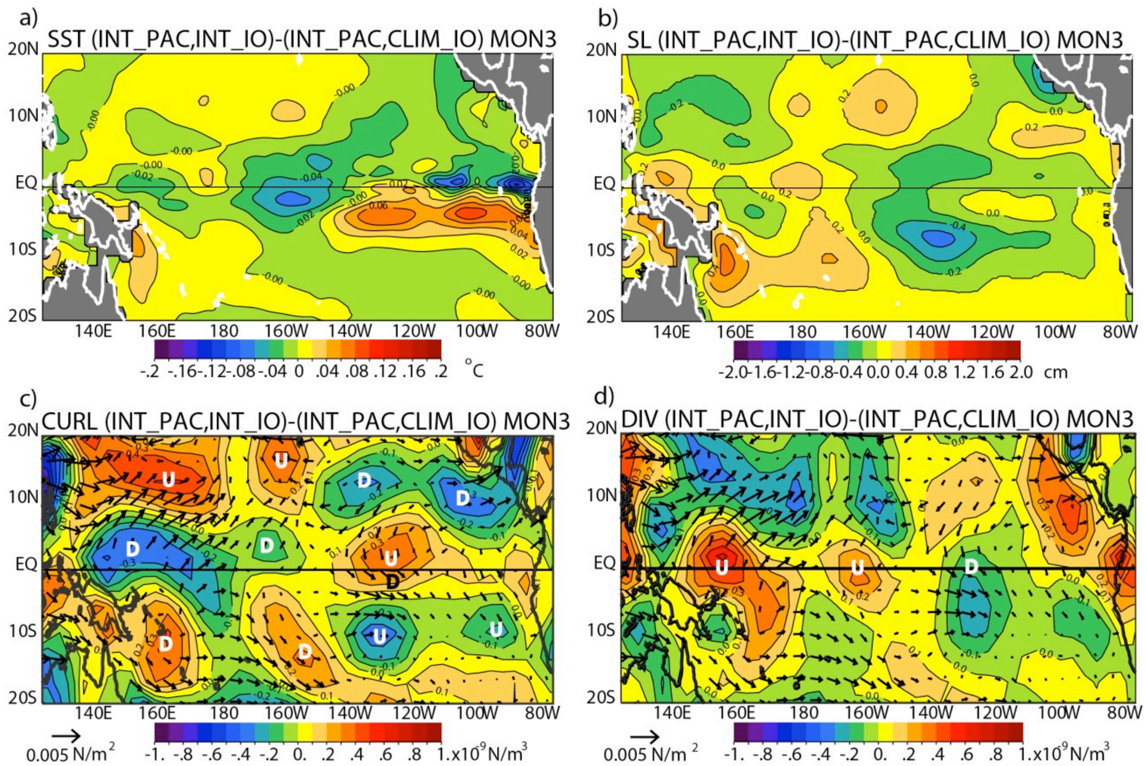

Figure 7: Average 3 month forecast INT_PAC, INT_IO - INT_PAC, CLIM_IO. Average forecast values for month 3 for a) SST, b) sea level, c) curl of the wind stress (color) and wind stress (vector), and d) divergence of the wind stress (color) and wind stress (vector). The scale of the vector plot is indicated in the bottom left of the panel. For the reader's convenience, regions of upwelling and downwelling are marked by letters U and D, respectively.

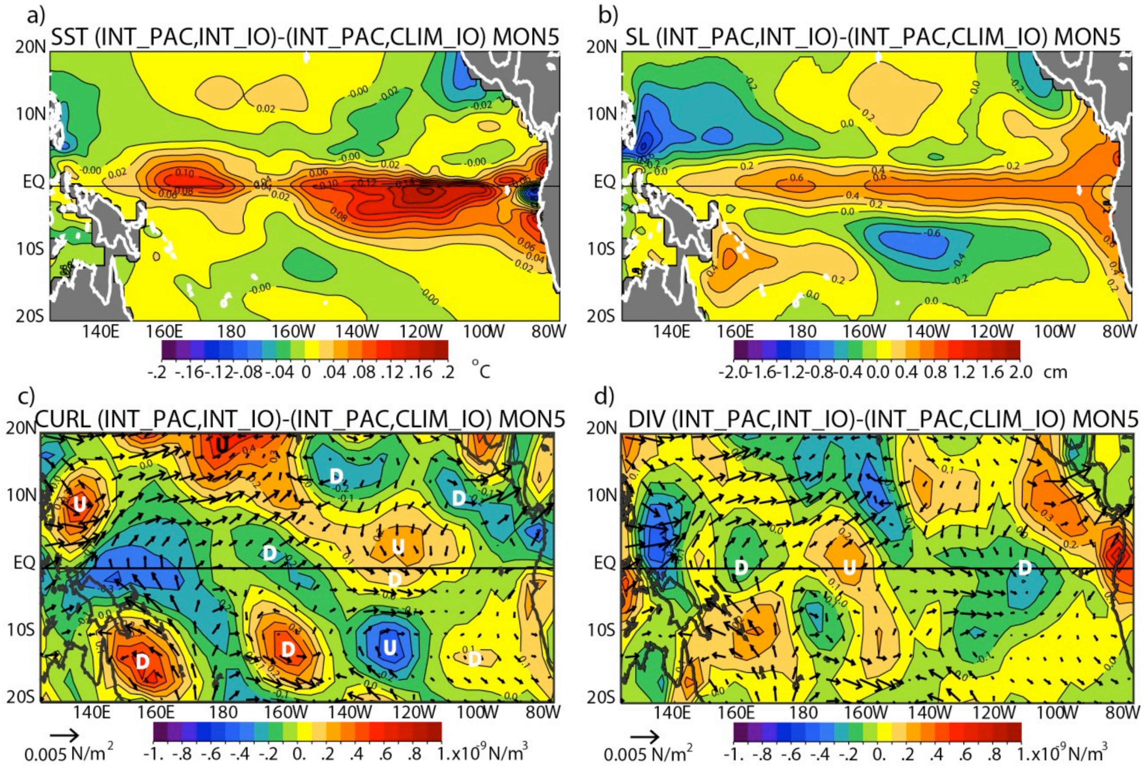

Figure 8: Average 5 month forecast INT_PAC, INT_IO - INT_PAC, CLIM_IO. Same as previous but for 5 month average forecasts.

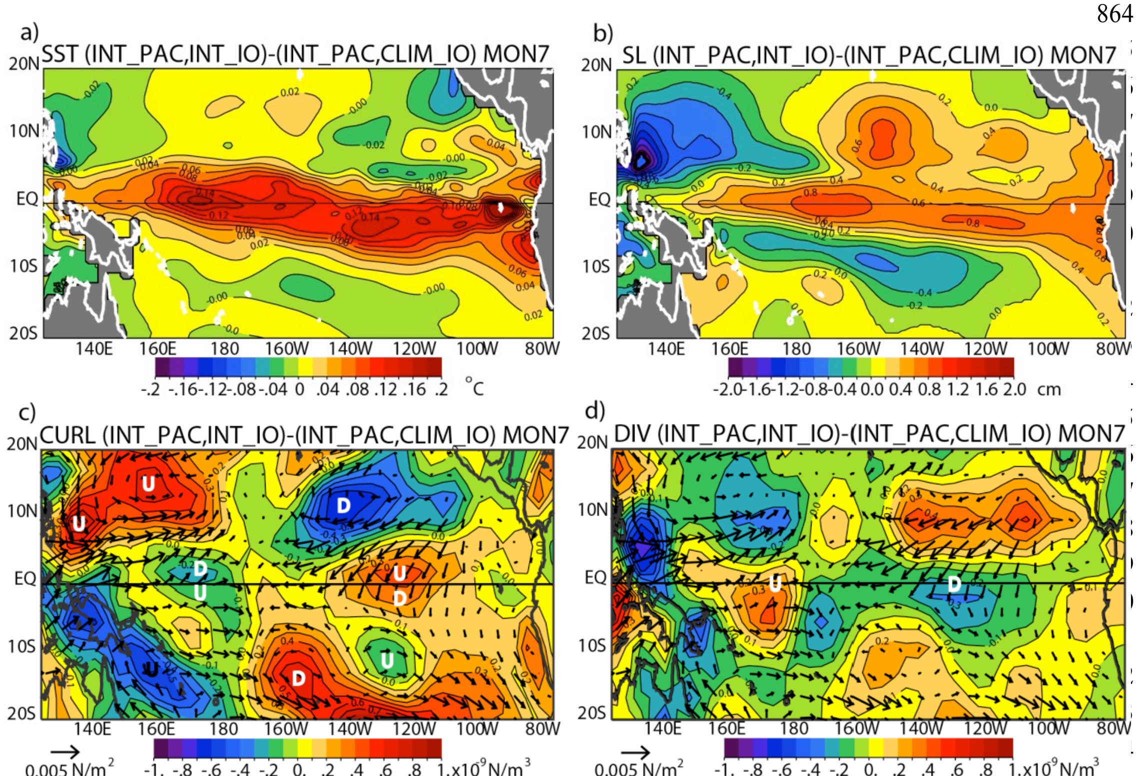

Figure 9: Average 7 month forecast INT_PAC, INT_IO - INT_PAC, CLIM_IO. Same as previous but for 7 month lead forecast mean.

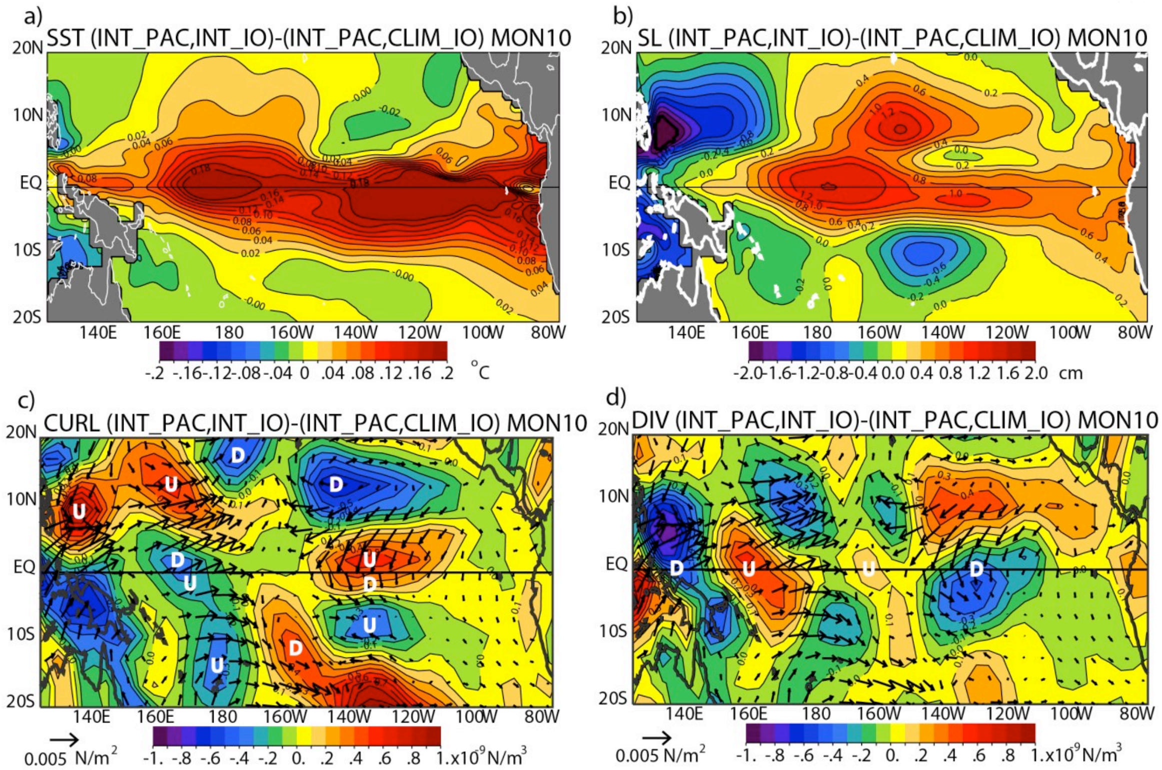

Figure 10: Average 10 month forecast INT_PAC, INT_IO - INT_PAC, CLIM_IO. Same as previous but for 10 month forecast mean.